JOURNAL OF CATALYSIS **171,** 358–373 (1997)
ARTICLE NO. CA971785

Kinetic Study of the CO Oxidation over Pt/γ-Al_2O_3 and Pt/Rh/CeO_2/γ-Al_2O_3 in the Presence of H_2O and CO_2

R. H. Nibbelke, M. A. J. Campman,[1] J. H. B. J. Hoebink,[2] and G. B. Marin[3]

Eindhoven University of Technology, Schuit Institute of Catalysis, Laboratorium voor Chemische Technologie, P.O. Box 513, 5600 MB, Eindhoven, The Netherlands

Received February 3, 1997; revised April 24, 1997; accepted May 29, 1997

The oxidation of CO by O_2 was studied for a Pt/γ-Al_2O_3 catalyst and for a commercially available Pt/Rh/CeO_2/γ-Al_2O_3 three-way catalyst. Kinetic experiments were carried out in an isothermal fixed-bed microreactor under intrinsic conditions, i.e., in the absence of mass and heat transfer limitations, in the temperature range from 436 to 503 K, with CO and O_2 inlet partial pressures between 0.12 and 8.3 kPa and H_2O and CO_2 inlet partial pressures between 0 and 10 kPa. For the Pt/γ-Al_2O_3 catalyst, the CO_2 production rate was found to be essentially proportional to the oxygen and inversely proportional to the carbon monoxide partial pressures, although at large CO and small O_2 partial pressures deviations occur. A kinetic model, based on elementary reaction steps, was constructed. It was concluded that for the experimental conditions considered, the noble metal surface is almost completely covered with CO, the CO adsorption being in quasi-equilibrium, and that irreversible molecular adsorption of oxygen is the rate-determining step, followed by potentially instantaneous dissociation. The presence of steam was found to enhance the reaction rate. For the experiments carried out over Pt/Rh/CeO_2/γ-Al_2O_3 in the presence 10 kPa H_2O and 10 kPa CO_2, it was found that the CO_2 production rate becomes zero order in CO at high CO partial pressures. The partial reaction order in O_2 is approximately 0.5. The experimental observations were explained by the existence of a second bifunctional reaction path next to the reaction path catalyzed by the noble metal only. The bifunctional reaction path involves a reaction between CO adsorbed on the noble metal and oxygen from ceria at the noble metal/ceria interface. The experiments could be described adequately over the investigated range of conditions by a kinetic model incorporating the mono- and bifunctional reaction paths. For the quantification and understanding of the changes in the partial reaction orders in CO and O_2 as a function of the experimental conditions, a kinetic model based on elementary reaction steps is necessary.

INTRODUCTION

Automotive exhaust catalysis for vehicles powered by Otto engines is aimed at the simultaneous treatment of three types of pollutants, i.e., carbon monoxide, hydrocarbons, and nitrogen oxides. For this purpose the so-called three-way catalyst was developed. Further improvements in the conversion of the pollutants are needed in order to meet the more stringent future standards. For that purpose, a full understanding of both the chemical and the physical aspects is necessary. Especially, there is an urgent need for realistic kinetic models based on reliable experimental data. In the present paper kinetic models based on elementary reaction steps are developed for the CO oxidation by O_2 in the presence of CO_2 and H_2O, the latter constituting a significant fraction of automotive exhaust.

The oxidation of CO by O_2 over group VIII metals has been studied extensively during the past decades. There seems to be general consensus on most of the elementary steps constituting the reaction mechanism. CO chemisorption on noble metals is generally considered to proceed molecularly via a precursor state (1); its adsorption and desorption kinetics have been addressed in detail (2–9). Oxygen adsorption was found to proceed dissociatively at temperatures above 100 K (5, 10), however, molecularly adsorbed oxygen is often included in reaction mechanisms (11, 12). This is substantiated physically by assuming that molecular chemisorption of oxygen is followed by potentially faster dissociation (8). Significant associative desorption of oxygen adatoms has not been observed at temperatures lower than 700 K (5, 10). The CO_2 formation step is still debated: it is thought to proceed via a Langmuir–Hinshelwood-type surface reaction or through an Eley–Rideal reaction between either dissociatively chemisorbed oxygen and gas phase CO or, conversely, molecularly chemisorbed CO and gas phase O_2. Before 1970 the Eley–Rideal mechanism predominated in the literature. Publications by Bonzel and Ku (13), Pacia *et al.* (14), and Golchet and White (15), in which the observations were explained by both Langmuir–Hinshelwood

[1] Current address: G.E. Plastics B.V., P.O. Box 117, 4600 AC, Bergen op Zoom, The Netherlands.

[2] Author to whom correspondence should be addressed. E-mail: margriet@chem.tue.nl.

[3] Current address: Universiteit Gent, Laboratorium voor Petrochemische Techniek, Krijgslaan 281, B-9000, Gent, Belgium.

0021-9517/97 $25.00

and Eley–Rideal steps, changed this predilection. Since the work of Engel and Ertl (3, 4) and Campbell *et al.* (16) the Langmuir–Hinshelwood mechanism prevails in the literature. Under atmospheric conditions, however, no conclusive evidence has yet been published that rules out the Eley–Rideal reaction step. CO oxidation by O_2 was found to proceed essentially via the same elementary steps over supported catalysts at atmospheric pressure as over single crystals under high-vacuum conditions (5, 17, 18). This result suggests that kinetic parameters for CO oxidation by O_2 obtained under high-vacuum conditions may be used as initial parameter estimates for modelling kinetic rate data obtained at atmospheric pressure. Studies conducted at atmospheric pressure are a minority in the vast number of publications regarding CO oxidation. Berlowitz *et al.* (19) and Cant *et al.* (12) described the kinetics using empirical rate equations while Voltz *et al.* (20) modeled the kinetics of CO oxidation in the presence of NO and C_3H_6 using empirical reaction rate equations with adsorption terms, but without taking into account the reaction between CO and NO. Herz and Marin (7) proposed a model using modified Langmuir–Hinshelwood mechanisms. Without kinetic parameter optimization the rate data measured by Schlatter and Chou (21) were simulated qualitatively. Subramaniam and Varma (22) performed a kinetic study using CO, NO, O_2, and H_2O. By kinetic parameter optimization a kinetic model was fitted to their data; however, this model was not based on elementary reaction steps. Montreuil *et al.* (23) carried out an extensive kinetic study using a full synthetic automotive exhaust and commercially available three-way catalysts, covering a wide range of reactant partial pressures at temperatures ranging from 640 to 900 K. The latter model, however, is not based on elementary steps either.

Nowadays, commercial three-way catalysts usually contain a certain amount of cerium oxide. Cerium oxide has been proved to improve the thermal stability of the support, increase the noble metal dispersion, and act as oxygen storage under oscillating conditions (24). The latter means that ceria stores oxygen under oxygen-rich conditions, and subsequently releases the stored oxygen under reducing conditions. Moreover, cerium oxide is known to influence the kinetics of reactions, e.g. the watergas-shift reaction and the CO oxidation. For Rh/ceria catalysts, a second reaction path for the oxidation of CO by O_2 involving both ceria and rhodium was suggested under reducing conditions, next to the reaction path catalyzed by the noble metal only (25, 26). This second reaction path consists of a reaction between CO adsorbed on Rh and oxygen from ceria, resulting in the experimentally observed zero partial reaction order in CO at high CO/O_2 ratios. The same conclusion was reached on the basis of temperature programmed desorption, TPD, studies (27, 28).

In the present paper, the CO oxidation by O_2 over $Pt/\gamma\text{-}Al_2O_3$ and $Pt/Rh/CeO_2/\gamma\text{-}Al_2O_3$ is studied. As the largest CO emission occurs during the so-called cold-start period, the study is carried out at temperatures below light-off of the converter. First, a kinetic model for the CO oxidation by O_2 over $Pt/\gamma\text{-}Al_2O_3$ is constructed. Next, the influence of steam on the CO oxidation over the latter catalyst is investigated. Based on the kinetic model for the "model catalyst" $Pt/\gamma\text{-}Al_2O_3$, a kinetic model is subsequently constructed for the CO oxidation over a commercially available $Pt/Rh/CeO_2/\gamma\text{-}Al_2O_3$ three-way catalyst in the presence of steam and carbon dioxide.

EXPERIMENTAL

Experimental Setup

The experimental setup consists of a feed, a reactor, and an on-line gas analysis section (29).

Feed section. The feed section consists of a gas blending manifold including a series of thermal gas massflow controllers and a HPLC pump to feed water to an evaporator located downstream of the flow controllers. Upstream of the flow controllers each gas supply line is secured by an electromagnetic valve. Downstream of the flow controllers the gases pass through a one-way valve prior to mixing. In order to prevent water condensation all lines and devices downstream of the water evaporators are heated to 373 K. The water evaporators are heated by a cylindrical oven. By heating the evaporator to 363 K a steady steam flow could be established. Water is pumped through an ejector into the evaporator. The downstream halves of the evaporators are filled with glass beads in order to prevent occasional drops of water from directly entering the reactor section. The upstream half does not contain beads so as to allow jet development from the nozzle. After passing through a valve arrangement the feed stream enters the reactor section.

Reactor section. The reactor section consists of a tubular preheater and a reactor which is contained in a cylindrical oven. The reactor employed is a stainless steel laboratory reactor containing the catalyst bed. The catalyst bed, retained by a sintered quartz plate, is diluted with nonporous $\alpha\text{-}Al_2O_3$ pellets of the same average diameter as the catalyst pellets in order to minimize temperature gradients in the reactor. A typical catalyst bed contained 0.2 g catalyst and 1.8 g diluent for the experiments with $Pt/\gamma\text{-}Al_2O_3$ and 0.5 g catalyst and 1.6 g diluent for the experiments with $Pt/Rh/CeO_2/\gamma\text{-}Al_2O_3$. The length of the catalyst bed is 10 mm and its diameter is 13 mm. The reactor inlet and outlet are filled with $\alpha\text{-}Al_2O_3$ beads, 1 mm in diameter, in order to maintain an isothermal catalyst bed and to enhance radial mixing of the inlet stream. The reactor is heated by two infrared radiators placed in line with the reactor, each at 85 mm from the reactor wall, and reactor and radiators are surrounded by a polished stainless steel canister with an inner diameter of 250 mm. Reactor pressure is manually

controlled by a spring loaded back pressure controller and measured downstream of the reactor. Methane, serving as an internal standard component for chemical analysis, is added to the reactor effluent directly downstream of the reactor. Subsequently, a fraction of the effluent, typically 150 ml/min, is directed to the gas analysis section. The remaining stream is passed through a water-cooled countercurrent steam condenser before being discharged to the exhaust line.

Gas analysis section. The on-line gas analysis section contains a gas chromatograph (Carlo Erba Instruments GC 8340) and a quadrupole mass spectrometer (VG Sensorlab 200D). The gas chromatographic analysis has been designed to enable on-line quantitative analysis of H_2, N_2, CO, NO, O_2, CO_2, and N_2O without interference of methane or steam. Separation of these components can be achieved using a Porapak R column using helium as carrier gas, in combination with a 500 μl sample loop. Separation of CO and O_2 requires a temperature as low as 245 K, using liquid carbon dioxide as a coolant. Water is separated by passing the sample stream through a Hayesep Q column at 343 K. Once the dried fraction of the sample has been passed to the Porapak column, the Hayesep column is purged with helium in a countercurrent way by an auxiliary stream of carrier gas in order to prevent breakthrough of water after successive runs. Downstream of the Porapak Q column the sample is analyzed by a thermal conductivity detector. In the present study, the quadrupole mass spectrometer was only used to verify stable water flow rate during the steady state experiments.

Catalysts

The catalysts used are Pt/γ-Al_2O_3 and Pt/Rh/CeO_2/γ-Al_2O_3. Catalyst samples were supplied in powder form by Degussa A.G. with an average powder diameter of 12 μm. The powder was pressed mechanically into pellets over 1 min with a pressure of 1 GPa. Subsequently, the pellets were crushed and sieved to obtain the desired fraction, which was $0.25 < d_p < 0.30$ mm for Pt/γ-Al_2O_3 and $0.15 < d_p < 0.21$ mm for Pt/Rh/CeO_2/γ-Al_2O_3. The desired particle size was chosen such that, on the one hand, a significant pressure drop over the catalyst bed was avoided and, on the other hand, significant internal concentration and temperature gradients could be neglected. The specific concentration of surface noble metal atoms, L_{NM} [$mol_s\ kg_{CAT}^{-1}$], was determined by CO chemisorption (Micromeretics ASAP) at 308 K. Prior to the chemisorption, the samples were pretreated *in situ*, similar to the samples used for the kinetic experiments. It was verified that at 308 K, no significant CO chemisorption occurred on the support. For the calculation of L_{NM}, 1 CO molecule per Pt and 2 per Rh surface atoms were assumed. The catalyst properties are summarized in Table 1.

TABLE 1

Properties of the Investigated Catalysts

Catalyst	Pt/γ-Al_2O_3	Pt/Rh/CeO_2/γ-Al_2O_3
α_s ($m^2\ kg_{CAT}^{-1}$)	225×10^3	125×10^3
d_p (m_p)	$0.25–0.30 \times 10^{-3}$	$0.15–0.21 \times 10^{-3}$
ρ_p ($kg_{CAT}\ m_p^{-3}$)	1230	2280
ε_p ($m_{gas}^3\ m_p^{-3}$)	0.67	0.67
L_{NM} ($10^{-3}\ mol_s\ kg_{CAT}^{-1}$)	8.0	1.4, 13.0[a]
w_{Pt} ($kg\ kg_{CAT}^{-1}$)	3.98×10^{-3}	3.98×10^{-3}
w_{Rh} ($kg\ kg_{CAT}^{-1}$)	—	7.98×10^{-4}
w_{CeO_2} ($kg\ kg_{CAT}^{-1}$)	—	2.8×10^{-1}

Note. α_s is the specific surface area, d_p the pellet diameter, ρ_p the pellet density, ε_p the pellet porosity, L_{NM} the specific concentration of surface noble metal atoms, and w_i the loading of component i.

[a] The first value is L_{NM} after and the second value is before *ex situ* pretreatment at 1173 K in air.

Catalyst Pretreatment

Prior to the experiments, the catalysts were pretreated in order to obtain reproducible kinetic data. For the Pt/γ-Al_2O_3 catalyst the pretreatment was as follows. The catalyst was heated to 773 K in a flow of 1.7×10^{-3} mol s^{-1} He. Then the catalyst was oxidized for 4 ks by a stream of 7.0×10^{-4} mol s^{-1} containing 27.5 kPa O_2 in He. Next, the catalyst was kept under a flow of 1.7×10^{-3} mol s^{-1} He at 773 K for 2 ks in order to purge reversibly adsorbed oxygen, followed by reduction in a stream of 8.84×10^{-4} mol s^{-1} containing 5.5 kPa H_2 in He at 773 K for 8 ks. Finally, the catalyst was allowed to cool down to reaction temperature under a He stream of 1.7×10^{-3} mol s^{-1}.

To simulate thermal aging, the Pt/Rh/CeO_2/γ-Al_2O_3 catalyst was first oxidized *ex situ* in stagnant air at 1173 K for 32 h, followed by the *in situ* pretreatment as described for Pt/γ-Al_2O_3 above. Next, the catalyst was allowed to cool down to reaction temperature under a flow of 8.15×10^{-4} mol s^{-1} containing 10 kPa H_2O and 10 kPa CO_2 in He.

Line-Out Procedure

For the Pt/γ-Al_2O_3 catalyst, it was found that the catalyst exhibited a higher initial activity after daily startup as compared to the activity measured after a few hours on stream. Therefore an *in situ* line-out procedure prior to the kinetic experiments was developed. The line-out procedure consisted of maintaining the following conditions for 3 h after startup:

$$p_{TOT} = 110\,\text{kPa},\ p_{CO}^0 = p_{O_2}^0 = 2.2\,\text{kPa},\ T = 473\,\text{K},$$
$$\text{and}\ \frac{W_{CAT}}{F_{CO}^0} = 15.5\,\text{kg}_{CAT}\,\text{s}\,\text{mol}^{-1},$$

where p_{TOT} is the total pressure [kPa], p_i^0 the inlet partial pressure of component i [kPa], T the temperature [K], W_{CAT}

the catalyst mass [kg_{CAT}], and F^0_{CO} the inlet molar flow rate of CO [mol s^{-1}]. For the experiments carried out over Pt/γ-Al_2O_3 in the presence of steam, $p^0_{H_2O}$ was set equal to 10 kPa and T equal to 483 K during the line-out. For a new batch of catalyst, the latter conditions had to be maintained for 15 h to reach a constant activity. After this initial line-out, a line-out of 1 h prior to the kinetic experiments was sufficient to reach stable activity. The reproducibility of the experiments was ensured by comparing the oxidation rate after the line-out procedure to that measured after a previous line-out.

For the Pt/Rh/CeO_2/γ-Al_2O_3 catalyst, the activity decreases monotonically as a function of time on stream. After 20 h on stream, the activity of the catalyst is only 30% of the initial activity. During the next 10 h the decrease is 10% or smaller, dependent on the temperature applied. Therefore, all experimental data were obtained within the latter period. This means that each new batch of catalyst was lined-out for 20 h after it was pretreated as described in the corresponding section. Next, experiments were carried out during a maximum period of 10 h. The line-out procedure consisted of maintaining a flow of 7.5×10^{-4} mol s^{-1} containing 10 kPa H_2O and 10 kPa CO_2 in He for 20 h at reaction temperature. If 0.80 kPa CO and 0.40 kPa O_2 also are fed during the line-out procedure, in order to monitor the catalyst activity, the decrease of the catalyst activity due to line-out is the same as that in the absence of CO and O_2. The decrease in activity is ascribed to irreversible deactivation. It seems unlikely that for the mild reaction conditions applied, sintering of noble metal or ceria can account for a 70% decrease of catalyst activity. A better explanation could be the formation of carbonate species on the ceria surface. Next to irreversible deactivation, the kinetic experiments with Pt/Rh/CeO_2/γ-Al_2O_3 are complicated by the fact that the activity measured for a given experimental condition depends on the recent history of the catalyst, i.e. the measured activity depends on the conditions applied prior to the experiment. Chemical changes of the catalyst, such as oxidation and reduction of ceria or of rhodium and the appearance and disappearance of crystal surfaces, are thought to be responsible for the latter observation. The importance of the dependence of the catalyst structure and composition on the experimental conditions was reported previously for automotive exhaust catalysts (30) and is referred to in the present paper as extrinsic relaxation. In order to obtain reproducible experimental data, a so-called standard condition was applied in between two subsequent experiments. The conditions corresponding to a given experiment were imposed for a period of only 10 min. Next, the standard condition was imposed for at least 30 min. In such a way catalyst changes due to extrinsic relaxation were avoided and changes in catalyst activity as compared to the activity at the standard condition were the result of the kinetics only. Indeed, following the above procedure, reproducible kinetic data could be obtained. The standard condition used for the experiments discussed in the present paper is as follows: $p^0_{CO} = 0.80$ kPa, $p^0_{O_2} = 0.40$ kPa, $p^0_{H_2O} = p^0_{CO_2} = 10$ kPa, $T = 436$ K, and $p_{TOT} = 110$ kPa. In all experiments, helium is used as a balance.

DATA EVALUATION

In the GC analysis, application of an internal standard, i.e., CH_4, allows quantification of the flow rates of the components in the product gas stream by relating the peak surface areas to the flow rate of the internal standard. For the Pt/γ-Al_2O_3 catalyst, the fractional conversions of CO and O_2 were calculated according to the normalization method, i.e., assuming 100% element balances. This allows calculation of the conversions from the outlet composition only. For each experiment it was assured that both the C- and O-balances were between 95 and 105%. For experiments carried out in the presence of steam, the O-balance and the fractional O_2 conversion were calculated assuming no net disappearance of H_2O. As nearly all experiments with Pt/Rh/CeO_2/γ-Al_2O_3 were carried out in the presence of H_2O and CO_2, conversions could only be calculated with the direct method, i.e. as the difference between the inlet and outlet flow rates divided by the inlet flow rate. Accurate measurements then could be guaranteed only if either the fractional CO or the O_2 conversion was larger than 0.10.

All experiments carried out with Pt/γ-Al_2O_3 were carried out differentially, i.e. the reaction rate can be regarded constant through the catalyst bed. Differential operating conditions could be assumed for fractional CO conversions smaller than 0.10. The net production rates then can be calculated directly from the measured conversions as

$$R_{w,i} = -\frac{X_i F_{TOT} p^0_i}{W_{CAT} p_{TOT}}, \qquad [1]$$

where $R_{w,i}$ is the production rate of component i [mol kg^{-1}_{CAT} s^{-1}]; X_i the fractional conversion of component i, defined as $X_i = (p^0_i - p^1_i)/p^0_i$; p^1_i is the partial pressures of component i at the reactor outlet [kPa]; and F_{TOT} is the total molar flow rate [mol s^{-1}].

In general, the experiments carried out with Pt/Rh/CeO_2/γ-Al_2O_3 are integral experiments, i.e. the influence of the changing gas composition along the reactor axis on the reaction rate cannot be neglected. To facilitate the qualitative interpretation of the results, however, the *mean* CO_2 production rates, also called space-time yields, were also calculated according to Eq. [1].

In order to measure intrinsic kinetics, the absence of significant internal and external concentration and temperature gradients on the scale of the catalyst particle was verified. On bed scale, it was confirmed that pressure drop over the catalyst bed and axial and radial temperature gradients could be neglected (29, 54). A typical value of the particle

based Reynolds number is 1. For all integral experiments, plug flow can be assumed and any effects of the dilution of the catalyst bed with inert α-Al_2O_3 on the measured conversion can be neglected.

MODELING

The degrees of surface coverage of the considered surface species were calculated from the corresponding continuity equations, which in the steady state can be represented as

$$\sum_{j=1}^{N} \nu_{i,j} r_{w,j} = 0, \qquad [2]$$

where j is the number of the reaction step, N the total number of reaction steps considered, $\nu_{i,j}$ the stoichiometric coefficient of surface species i in reaction step j, and $r_{w,j}$ the reaction rate of reaction step j [mol kg_{CAT}^{-1} s^{-1}]. The reaction rates of the elementary reaction steps are calculated via the law of mass action and under the Langmuir assumptions of identical active sites, absence of interactions between adsorbates, and confinement of adsorption to a monolayer. Equation [2] forms a set of algebraic equations with the degrees of surface coverage of the considered surface species as only unknowns for a given gas phase composition, pressure, and temperature. For the kinetic models discussed in the present paper, this set of algebraic equations could be solved analytically, either by hand or by Maple V (31). Subsequently, the CO_2 production rate can be calculated from the degrees of surface coverage. For the experiments carried out with Pt/γ-Al_2O_3, the calculated CO_2 production rate can be compared directly to the experimental value.

For the integral experiments carried out with Pt/Rh/CeO_2/γ-Al_2O_3, a reactor model must be considered in combination with a kinetic model. Since the fixed-bed reactor can be regarded as an ideal plug flow reactor, the fractional CO conversion can be calculated by integration of the ordinary differential equation,

$$\frac{dX_{CO}}{dz} = -\frac{W_{CAT}\, p_{TOT}}{F_{TOT}\, p_{CO}^0} R_{w,CO}, \qquad [3]$$

where z is the dimensionless reactor length, defined as the cumulative catalyst mass divided by the total catalyst mass. The initial condition corresponding to Eq. [3] is that $X_{CO} = 0$ for $z = 0$. Equation [3] was integrated using a backward differentiation formula, BDF, integrator from the NAG Fortran library (32), routine D02NHF.

REGRESSION ANALYSIS

Estimation of the kinetic parameters was performed by minimization of the objective function

$$S(\mathbf{b}) = \sum_{i=1}^{n} [y_i - g(\mathbf{x}_i, \mathbf{b})]^2 \rightarrow \text{minimum}, \qquad [4]$$

where S is the objective function; $\mathbf{b}$ the parameter vector; y_i the ith experimental observation, which is the CO_2 production rate for the experiments with Pt/γ-Al_2O_3 and the fractional CO conversion for the experiments with Pt/Rh/CeO_2/γ-Al_2O_3; $g(\mathbf{x}_i, \mathbf{b})$ the corresponding value calculated by the model; $\mathbf{x}_i$ the vector of set variables for experiment i; and n the number of experiments. The objective function is based upon the assumption that the experimental errors are normally distributed with a zero mean. The minimization of the objective function was achieved with a single-response Levenberg–Marquardt algorithm (33, 34).

The parameter estimates were tested for statistical significance on the basis of their individual t-values. If not all parameters could be estimated in a statistically significant way, the model was simplified in order to obtain statistically significant parameter estimates only. The statistical significance of the global regression was expressed by means of the so-called F-test, which is based on the comparison of the sum of squares of the calculated response values and the residual sum of squares. A high F-value corresponds to a high significance of the global regression. Discrimination among rival models was based on this statistical testing, whenever it was not possibly by direct observation or by physico-chemical laws. In order to avoid strong binary correlation between the Arrhenius parameters, the Arrhenius equations were reparametrized according to Kitrell (35).

EXPERIMENTAL RESULTS

CO Oxidation over Pt/γ-Al_2O_3

The range of experimental conditions covered is listed in Table 2. The range includes reactant partial pressures and temperatures encountered in realistic automotive exhaust catalysis during the cold-start period.

The CO_2 production rate decreases monotonically at increasing CO partial pressure, indicating that the reaction is inhibited by CO. Even at $p_{CO}/p_{O_2}|_0$ as low as 0.01, the reaction rate decreased with increasing CO partial pressure. An

TABLE 2

Range of Experimental Conditions during the CO Oxidation over Pt/γ-Al_2O_3 in the Absence and in the Presence of Steam. Helium Is Used as a Balance

	Absence of steam	Presence of steam
p_{TOT} (kPa)	110	110
p_{CO}^0 (kPa)	0.22–8.3	0.88–4.4
$p_{O_2}^0$ (kPa)	0.37–8.3	0.44–4.4
$p_{CO}/p_{O_2}\|_0$	0.1–3	0.33–7.7
$p_{H_2O}^0$ (kPa)	0	0–10
T (K)	463–503	463–503

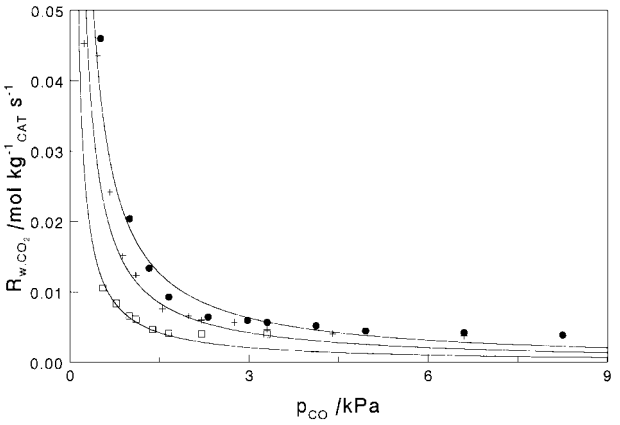

FIG. 1. CO_2 production rate vs p_{CO} over Pt/γ-Al_2O_3 at $T = 483$ K. (□) $p_{O_2} = 1.1$ kPa; (+) $p_{O_2} = 2.2$ kPa; (●) $p_{O_2} = 3.3$ kPa. Markers represent the experiments. Solid lines are calculated with Eq. [13] and the parameter values are given in Table 5.

example of the CO_2 production rate versus the CO partial pressure is shown in Fig. 1.

The CO_2 production rate is proportional to the O_2 partial pressure, except at small oxygen partial pressures, where a smaller order in O_2 is observed. An example of the CO_2 production rate versus the O_2 partial pressure is shown in Fig. 2.

For the experimental conditions under consideration, the CO_2 partial pressure does not significantly affect the CO_2 production rate, which is in agreement with results published by Conrad *et al.* (36), Campbell *et al.* (16), and Solymosi (37). Indeed, the variety of elementary steps proposed for the noble metal catalyzed oxidation of CO do not include CO_2 interaction with the noble metal.

Figure 3 shows the effect of the steam partial pressure on the CO_2 production rate for fixed CO and O_2 partial pressures. The presence of steam enhances the CO_2 production rate, the effect being most pronounced at low steam partial pressures. At steam partial pressures larger than 1 kPa, the partial reaction order in H_2O becomes zero. Because of the low reaction temperatures, the CO conversion due to the watergas-shift reaction can be expected to be negligible (38, 55). Indeed, at the temperatures applied no CO_2 production was found in the absence of O_2, although the latter does not rule out the absence of the watergas-shift reaction completely as the catalyst structure may be different in the absence as compared to in the presence of oxygen. Figure 4 shows the CO_2 production rate as a function of the CO partial pressure in both the absence and the presence of steam. The partial reaction order in CO is not altered by the presence of steam. The same holds for the dependence of the CO_2 production rate on the O_2 partial pressure. At higher

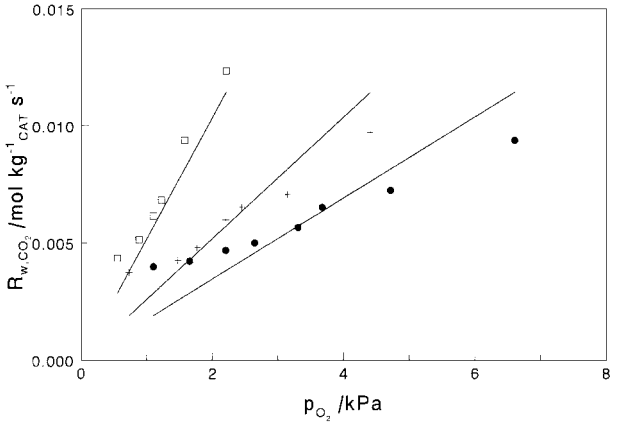

FIG. 2. CO_2 production rate vs p_{O_2} over Pt/γ-Al_2O_3 at $T = 483$ K. (□) $p_{CO} = 1.1$ kPa; (+) $p_{CO} = 2.2$ kPa; (●) $p_{CO} = 3.3$ kPa. Markers represent the experiments. Solid lines are calculated with Eq. [13] and the parameter values are given in Table 5.

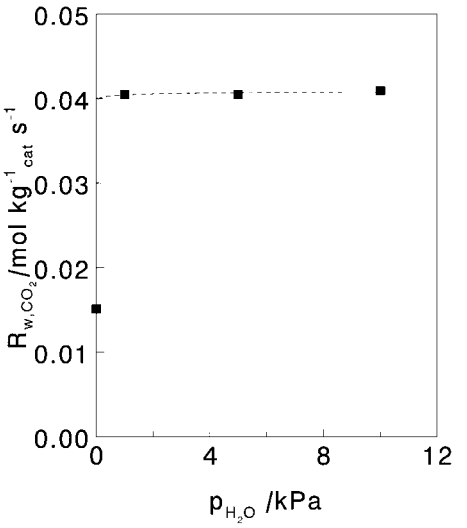

FIG. 3. CO_2 production rate vs p_{H_2O} over Pt/γ-Al_2O_3. $p_{CO} = 0.88$ kPa, $p_{O_2} = 2.2$ kPa, $T = 483$ K. Note the datapoint at $p_{H_2O} = 0$ kPa. The dashed line is only shown to guide the eye.

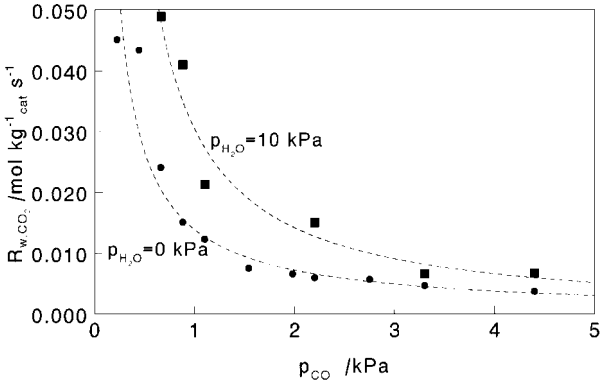

FIG. 4. CO_2 production rate vs p_{CO} over Pt/γ-Al_2O_3 for $p_{H_2O} = 0$ kPa (●) and $p_{H_2O} = 10$ kPa (■). $p_{O_2} = 2.2$ kPa, $T = 483$ K. Dashed lines are only shown to guide the eye.

TABLE 3

Range of Experimental Conditions during the CO Oxidation over Pt/Rh/CeO_2/γ-Al_2O_3 in the Presence of Steam and Carbon Dioxide. Helium Is Used as a Balance

p_{TOT} (kPa)	110
p^0_{CO} (kPa)	0.12–4.0
$p^0_{O_2}$ (kPa)	0.12–2.5
$p_{CO}/p_{O_2}\|_0$	0.13–16
$p^0_{H_2O}$ (kPa)	10
$p^0_{CO_2}$ (kPa)	10
T (K)	436

temperatures, the rate enhancement due to the presence of steam decreases.

CO Oxidation over Pt/Rh/CeO_2/γ-Al_2O_3 in the Presence of Steam and Carbon Dioxide

The range of experimental conditions covered is listed in Table 3. The experiments were carried out at a lower temperature as compared to the experiments carried out with Pt/γ-Al_2O_3 because of the difficulty of measuring intrinsic kinetics with the more active Pt/Rh/CeO_2/γ-Al_2O_3 catalyst at higher temperatures.

Most experiments were carried out at constant inlet partial pressures of H_2O and CO_2 equal to 10 kPa to simulate a more realistic automotive exhaust. In Fig. 5a, the CO conversion versus the CO inlet partial pressure is shown. To facilitate the interpretation of the data, in Fig. 5b the same data are depicted as the space-time yield, calculated from Eq. [1], versus the CO inlet partial pressure. As the measurements are integral, the exact partial reaction order cannot be calculated. The partial reaction order in CO is negative for low p_{CO}, although less negative as compared to Pt/γ-Al_2O_3, i.e., approximately -0.3 instead of -1. At large values of p_{CO} the partial reaction order becomes zero. The latter observation is in accordance with previous studies carried out with Rh/CeO_2 (25, 26, 39), Pt/CeO_2, and Pd/CeO_2 catalysts (40), and can be explained by the existence of a second, bifunctional, reaction path next to the reaction path catalyzed by the noble metal only. This bifunctional reaction path involves a reaction between CO adsorbed on the noble metal surface and oxygen from ceria, as was already discussed in the Introduction.

In Fig. 6a, the CO conversion versus the O_2 inlet partial pressure is shown. In Fig. 6b, the same data are again depicted as the space-time yield versus the O_2 inlet partial pressure. The partial reaction order in O_2 is smaller than for the Pt/γ-Al_2O_3 catalyst, i.e., approximately 0.5 instead of 1. The decrease of the reaction order in O_2 is in agreement with previous studies (25, 40) and can also be explained by the existence of a bifunctional reaction path, as will become clear during the discussion of the modeling results.

Because of the low reaction temperature, i.e., 436 K, the contribution of the watergas-shift reaction to the conversion of CO can be expected to be negligible, as was also the case for the experiments over Pt/γ-Al_2O_3 in the presence of steam. Indeed, experiments carried out in the absence of oxygen showed significant CO_2 production rates, as compared to the experiments in the presence of oxygen, at temperatures above 500 K only. Because a standard condition is applied in between two subsequent experiments, it can be expected that the catalyst structure for the experiments in the absence as compared to that in the presence of oxygen is the same.

In Fig. 7, the influence of the steam and carbon dioxide partial pressures on the CO conversion is shown. The presence of steam enhances the CO_2 production rate, as was also the case for the Pt/γ-Al_2O_3 catalyst. In contrast to

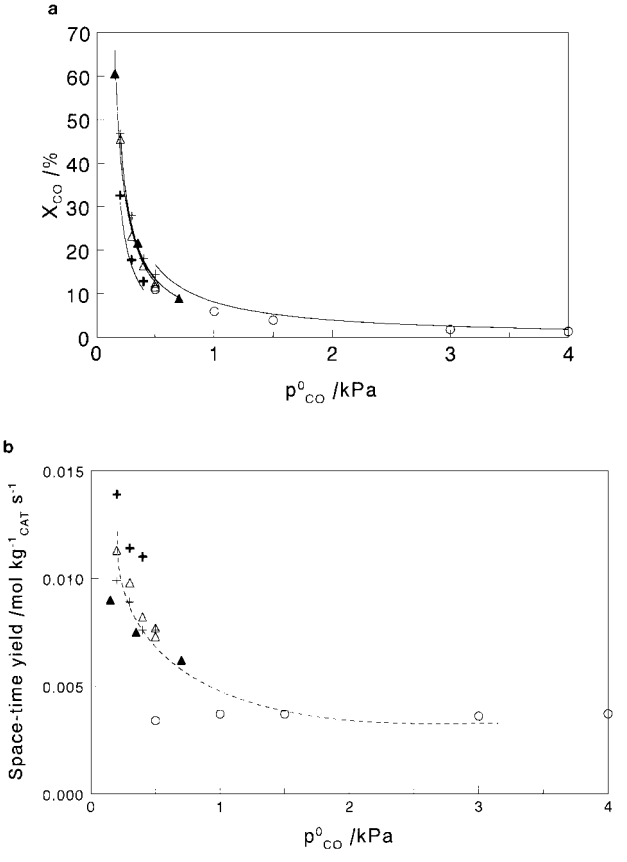

FIG. 5. (a) CO conversion and (b) space-time yield vs CO inlet partial pressure over Pt/Rh/CeO_2/γ-Al_2O_3 at 436 K for $p^0_{H_2O} = p^0_{CO_2} =$ 10 kPa. (○) $p^0_{O_2} = 0.25$ kPa, $W_{CAT} = 0.4375$ g, $F_{TOT} = 3.0$ mmol s^{-1}; (▲) $p^0_{O_2} = 0.70$ kPa, $W_{CAT} = 0.5046$ g, $F_{TOT} = 5.5$ mmol s^{-1}; (+) $p^0_{O_2} =$ 1.0 kPa, $W_{CAT} = 0.4311$ g, $F_{TOT} = 5.0$ mmol s^{-1}; (△) $p^0_{O_2} = 1.5$ kPa, $W_{CAT} =$ 0.4375 g, $F_{TOT} = 6.0$ mmol s^{-1}; (+) $p^0_{O_2} = 2.1$ kPa, $W_{CAT} = 0.2989$ g, $F_{TOT} =$ 7.0 mmol s^{-1}. Markers represent the experiments. The solid lines in (a) were calculated with the parameter values given in Table 7 by integration of Eq. [3] with Eq. [13] and Eq. [24] for the production rates. The dashed line in (b) is only shown to guide the eye.

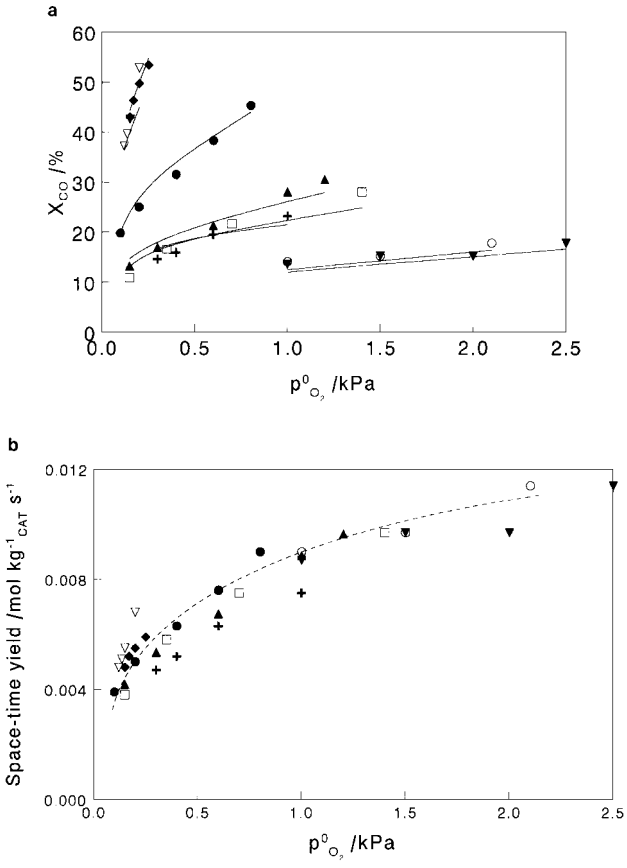

FIG. 6. (a) CO conversion and (b) space-time yield vs O_2 inlet partial pressure over Pt/Rh/CeO_2/γ-Al_2O_3 at $T = 436$ K for $p^0_{H_2O} = p^0_{CO_2} =$ 10 kPa. (▽) $p^0_{CO} = 0.12$ kPa, $W_{CAT} = 0.6123$ g, $F_{TOT} = 7.2$ mmol s^{-1}; (◆) $p^0_{CO} = 0.15$ kPa, $W_{CAT} = 0.6123$ g, $F_{TOT} = 5.0$ mmol s^{-1}; (●) $p^0_{CO} = 0.20$ kPa, $W_{CAT} = 0.6590$ g, $F_{TOT} = 7.2$ mmol s^{-1}; (○) $p^0_{CO} = 0.30$ kPa, $W_{CAT} = 0.2989$ g, $F_{TOT} = 7.0$ mmol s^{-1}; (▲) $p^0_{CO} = 0.30$ kPa, $W_{CAT} = 0.4311$ g, $F_{TOT} = 5.0$ mmol s^{-1}; (▼) $p^0_{CO} = 0.35$ kPa, $W_{CAT} = 0.2989$ g, $F_{TOT} = 6.0$ mmol s^{-1}; (□) $p^0_{CO} = 0.35$ kPa, $W_{CAT} = 0.5046$ g, $F_{TOT} = 5.5$ mmol s^{-1}; (+) $p^0_{CO} = 0.60$ kPa, $W_{CAT} = 0.5046$ g, $F_{TOT} = 3.0$ mmol s^{-1}. Markers represent the experiments. The solid lines in (a) were calculated with the parameter values given in Table 7 by integration of Eq. [3] with Eq. [13] and Eq. [24] for the production rates. The dashed line in (b) is only shown to guide the eye.

Pt/γ-Al_2O_3, carbon dioxide inhibits the CO oxidation. For the values of $p^0_{H_2O}$ and $p^0_{CO_2}$ corresponding to Figs. 5 and 6, i.e., 10 kPa, the dependence of the CO conversion on the H_2O and CO_2 partial pressures is small. Therefore, H_2O and CO_2 need not be considered explicitly in modeling the CO oxidation over Pt/Rh/CeO_2/γ-Al_2O_3 in the presence of 10 kPa steam and 10 kPa carbon dioxide.

MODELING RESULTS

CO Oxidation over Pt/γ-Al_2O_3

A kinetic model based on elementary steps was developed for the experiments carried out with Pt/γ-Al_2O_3 in the absence of steam. The reaction paths considered and

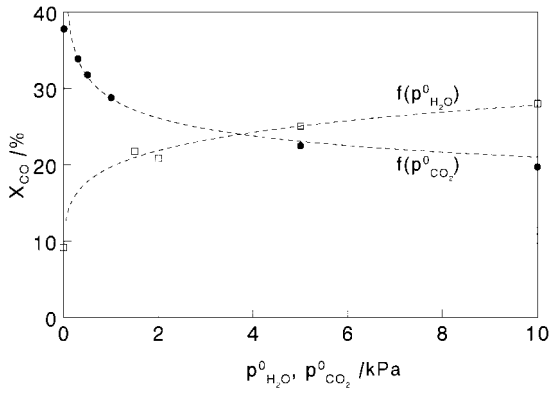

FIG. 7. CO conversion vs H_2O (□) and CO_2 (●) inlet partial pressures over Pt/Rh/CeO_2/γ-Al_2O_3 at 436 K. (□) $p^0_{CO_2} = 10$ kPa, $p^0_{CO} = 0.15$ kPa, $p^0_{O_2} = 0.20$ kPa; (●) $p^0_{H_2O} = 10$ kPa, $p^0_{CO} = 0.20$ kPa, $p^0_{O_2} = 0.20$ kPa. Dashed lines are only shown to guide the eye.

the corresponding elementary steps are listed in Table 4, where the stoichiometric numbers σ of the reactions express the number of times each reaction has to proceed for the corresponding closed sequence to turn over once (41). Each reaction path consists of a closed sequence of elementary steps, the choice of elementary steps from the variety of steps reported in literature being based on the observed dependencies of R_{w,CO_2} on the conditions. Steps (2-f), (2-b), and (3) have been adopted to allow for the direct proportionality between the rate of oxygen adsorption and the fraction of vacant active sites (17), despite the fact that molecularly adsorbed oxygen has not been reported under

TABLE 4

Elementary Step Reaction Paths Considered in the Kinetic Modeling of CO Oxidation by O_2 over Pt/γ-Al_2O_3 in the Absence of Steam. Each Reaction Path A to F Consists of $\{\sigma_{\text{step 1}}, \ldots, \sigma_{\text{step 6}}\}$ Where $\sigma_{\text{step } i}$ Is the Stoichiometric Number for Step i

Elementary step	Reaction path A	B	C	D	E	F	Step number
	σ_A	σ_B	σ_C	σ_D	σ_E	σ_F	
$CO + * \underset{k_1^b}{\overset{k_1^f}{\rightleftarrows}} CO^*$	2	0	2	0	2	0	(1)
$O_2 + * \xrightarrow{k_2^f} O_2^*$	1	1	1	1	0	0	(2-f)
$O_2^* \xrightarrow{k_2^b} O_2 + *$	0	0	1	1	0	0	(2-b)
$O_2^* + * \xrightarrow{k_3^f} 2O^*$	1	1	1	1	0	0	(3)
$O_2 + 2^* \xrightarrow{k_4^f} 2O^*$	0	0	1	1	1	1	(4)
$CO^* + O^* \xrightarrow{k_{LH}} CO_2 + 2^*$	2	0	2	0	2	0	(5)
$CO + O^* \xrightarrow{k_{ER}} CO_2 + *$	0	2	0	2	0	2	(6)
$2CO + O_2 \rightarrow 2CO_2$	+						

the experimental conditions (5). In step (4) the backward reaction, associative desorption of oxygen, has been omitted since no significant associative desorption of oxygen has been reported for the process conditions applied in this study. Except for the reaction steps describing molecular chemisorption of O_2 followed by its dissociation, these elementary steps are among the most frequently reported (4, 8, 16, 42–44). Based on the reaction paths A to F in Table 4, six rate expressions can be derived. The rate coefficients are defined such that the corresponding reaction rate is obtained in the unit mol mol_s^{-1} s^{-1}, i.e., as a turnover frequency. The latter must be multiplied by the specific concentration of active sites L_{NM} [mol_s kg_{CAT}^{-1}], given in Table 1, to enable comparison with the experimentally measured specific rates in mol kg_{CAT}^{-1} s^{-1}.

Reaction Path A

In reaction path A from Table 4, oxygen adsorption is thought to proceed in two steps in series, first the irreversible molecular chemisorption of O_2 followed by the dissociation of O_2^*, steps (2-f) and (3) in Table 4. CO_2 formation takes place via a Langmuir–Hinshelwood surface reaction. The continuity equations for the CO, O_2, and O surface species are respectively

$$k_1^f p_{CO}\theta_* - k_1^b\theta_{CO} - k_{LH}\theta_{CO}\theta_O = 0 \quad [5]$$

$$k_2^f p_{O_2}\theta_* - k_3^f\theta_{O_2}\theta_* = 0 \quad [6]$$

and

$$2k_3^f\,\theta_{O_2}\,\theta_* - k_{LH}\,\theta_O\theta_{CO} = 0, \quad [7]$$

where θ_i is the degree of surface coverage of component i, defined as the amount of adsorbed species i divided by a monolayer capacity, i.e., L_{NM} [mol kg_{CAT}^{-1}]. θ_* is the fraction of empty sites and follows from the site balance:

$$\theta_{CO} + \theta_{O_2} + \theta_O + \theta_* = 1 \quad [8]$$

If, subsequently, the solutions for θ_{CO} and θ_O are substituted in the rate equation

$$R_{w,CO_2} = k_{LH}\,L_{NM}\,\theta_{CO}\,\theta_O, \quad [9]$$

the following rate expression is obtained:

$$R_{w,CO_2} = \frac{2k_1^b k_2^f L_{NM} p_{O_2}\left(k_1^f k_{LH} k_3^f p_{CO} - k_1^f k_{LH} k_2^f p_{CO} p_{O_2} - 2k_1^b k_3^f k_2^f p_{O_2} + 2{k_2^f}^2 k_{LH} p_{O_2}^2 - 2k_{LH} k_3^f k_2^f p_{O_2}\right)}{k_{LH} k_3^f \left(k_1^f p_{CO} + k_1^b - 2k_2^f p_{O_2}\right)\left(k_1^f p_{CO} - 2k_2^f p_{O_2}\right)}. \quad [10]$$

Assuming CO adsorption equilibrium leads to

$$R_{w,CO_2} = \frac{2k_2^f L_{NM} p_{O_2}\left(k_{LH} K_1 k_3^f p_{CO} - 2k_2^f k_3^f p_{O_2} - k_{LH} K_1 k_2^f p_{CO} p_{O_2}\right)}{k_{LH} k_3^f K_1 p_{CO}(1 + K_1 p_{CO})}, \quad [11]$$

where $K_1 = k_1^f / k_1^b$ is the equilibrium coefficient of CO adsorption.

If O_2 chemisorption, step (2-f), is considered to be rate determining, implying $\theta_{O_2} \ll \theta_O \ll \theta_*$, the rate expression is simplified to

$$R_{w,CO_2} = \frac{2k_2^f L_{NM} p_{O_2}}{1 + K_1 p_{CO}}. \quad [12]$$

According to the formal definition of a rate-determining step, it is required that all steps but the one denoted as rate determining are at quasi-equilibrium, i.e. their affinity is approximately zero. If more than one step has a nonzero affinity, as is the case for reaction path A, this definition cannot be strictly applied. However, Boudart and Tamaru (45) provided the following operational definition for the rate-determining step: for an irreversible catalytic cycle, the rate-determining step is the only step whose forward rate coefficient appears in the rate equation. For a reversible catalytic cycle, the rate-determining step is the only step for which both the forward and the backward rate coefficients appear in the rate equation.

If it is assumed that CO^* is the most abundant reaction intermediate, i.e., $\theta_{CO} \gg \theta_*$, Eq. [12] reduces to

$$R_{w,CO_2} = \frac{2k_2^f L_{NM}}{K_1}\frac{p_{O_2}}{p_{CO}}. \quad [13]$$

Reaction Path B

In path B oxygen chemisorption and dissociation proceed similarly to path A. The reaction takes place via the Eley–Rideal step between adsorbed oxygen and gas-phase CO, step (6) in Table 4. Note that adsorbed CO does not take part in the formation of CO_2, hence the establishment of adsorption equilibrium for CO is evident. Assuming that molecular chemisorption of oxygen is rate determining and, additionally, that CO^* is the most abundant reaction intermediate leads to the same rate expressions that were found for reaction path A, Eqs. [12] and [13]. This is obvious, since paths A and B only differ as far as the surface reaction step is concerned. By the simplifying assumptions the surface reaction step is rendered kinetically insignificant. This indicates that no discrimination between a Langmuir–Hinshelwood step and an Eley–Rideal step can be made on the basis of the simplified models from reaction paths A and B.

Reaction Paths C and D

Reaction paths C and D correspond to paths A and B, respectively, the difference being that now desorption of

molecularly chemisorbed oxygen is taken into account. In the case of adsorption equilibrium for CO and O_2, if dissociation of O_2^*, step (3) in Table 4, is considered to be rate determining, and if CO^* is assumed to be the most abundant reaction intermediate, the following rate expression is obtained for both reaction paths C and D:

$$R_{w,CO_2} = \frac{2k_3^f K_2 L_{NM}}{K_1^2} \frac{p_{O_2}}{p_{CO}^2}. \quad [14]$$

Again, to discrimination between a Langmuir–Hinshelwood or an Eley–Rideal reaction is possible, because the reaction step is not kinetically significant.

Reaction Paths E and F

Reaction paths E and F correspond to paths A and B, respectively, the difference being that dissociative oxygen adsorption is thought to proceed in one elementary step. In the case of adsorption equilibrium for CO, if oxygen adsorption is assumed to be rate determining, and if CO^* is assumed to be the most abundant reaction intermediate, the following rate expression is obtained for both reaction paths E and F:

$$R_{w,CO_2} = \frac{2k_4^f L_{NM}}{K_1^2} \frac{p_{O_2}}{p_{CO}^2}. \quad [15]$$

The most important phenomenological difference between the simplified rate equations for reaction paths A and B, Eq. [13], for reaction paths C and D, Eq. [14], and for reaction paths E and F, Eq. [15], is that in Eq. [13] the CO_2 production rate is inversely proportional to p_{CO}, while in Eqs. [14] and [15] this rate is inversely proportional to p_{CO}^2.

The kinetic parameters appearing in the rate expressions presented above may be estimated from collision theory and transition state theory. The rate coefficients can be described in an Arrhenius form as

$$k_i = A_i \exp\left[\frac{-E_{a,i}}{RT}\right], \quad [16]$$

where A_i is the preexponential factor, $E_{a,i}$ the activation energy [J mol^{-1}] of the rate coefficient k_i, R the gas constant [J mol^{-1} K^{-1}], and T the temperature [K].

The equilibrium coefficients therefore can be expressed as

$$K_i = \frac{A_i^f}{A_i^b} \exp\left[\frac{-\Delta H_i^0}{RT}\right], \quad [17]$$

where ΔH_i^0 is the standard reaction enthalpy of reaction i [J mol^{-1}].

Preexponential factors based on theoretical considerations are often presented as ranges of feasible values. Therefore they can only serve as initial parameter estimates for kinetic modeling purposes, rather than being accurate predictions. From collision theory the rate coefficient of chemisorption in units of mol mol$_{Pt}^{-1}$ Pa^{-1} s^{-1} is expressed as

$$k_{ads} = (2\pi MRT)^{1/2} s_0 \sigma, \quad [18]$$

where M is the molar mass of the chemisorbing species [kg mol^{-1}], s_0 the sticking probability, and σ the atomic surface area [m^2 mol$_{Pt}^{-1}$]. The dependence of the sticking probability s_0 on temperature can be described by an Arrhenius equation. Molecular chemisorptions of CO and O_2 have been reported to be essentially nonactivated processes (Refs. (2, 4) and (13, 18), respectively). For dissociative chemisorption, Herz and Marin (7) assume a small negative activation energy amounting to -4.2 kJ mol^{-1}.

The main result of the regression analysis is that, under the wide range of experimental conditions applied in this study, the assumptions of CO adsorption equilibrium and of CO^* being the most abundant reaction intermediate are valid. This means that all experiments in this study have been carried out at CO coverages close to unity. Regression using models without these assumptions did not result in statistically significant parameter estimates. This indicates that under conditions relevant to automotive catalysis at temperatures below light-off, steady-state CO oxidation by O_2 over Pt/γ-Al_2O_3 can be described using fairly simple algebraic rate expressions such as

$$R_{w,CO_2} = A^{global} \exp\left[\frac{-E_a^{global}}{RT}\right] L_{NM} f(p_{CO}, p_{O_2}), \quad [19]$$

in which $f(p_{CO}, p_{O_2})$ is described by Eq. [20] for reaction paths A and B,

$$f(p_{CO}, p_{O_2}) = \frac{p_{O_2}}{p_{CO}}, \quad [20]$$

and by Eq. [21] for reaction paths C, D, E, and F.

$$f(p_{CO}, p_{O_2}) = \frac{p_{O_2}}{p_{CO}^2}. \quad [21]$$

In the parameters A^{global} and E_a^{global} in Eq. [19] the preexponential factors and temperature dependencies of the individual processes are lumped, indicating that the physical interpretation of these parameters depends on the model considered. The F-values for Eqs. [20] and [21] are respectively 1347 and 223, using 129 experiments for the regression analysis. Thus, considering the F-values, Eq. [20] describes the experimental results more adequately than does Eq. [21]. Equation [20] corresponds to the rate equation [13] for reaction paths A and B, where molecular adsorption of oxygen is considered rate determining, and CO^* is the most abundant reaction intermediate. The physical interpretation of A^{global} and E_a^{global} according to Eq. [13] and

TABLE 5

Physical Interpretation and Estimates of the Global Preexponential Factor and Activation Energy with Their 95% Confidence Intervals Obtained by Regression of the Experimental Data Obtained in the Absence of Steam over Pt/γ-Al_2O_3 with Eq. [13]

$A^{\text{global}} = 2k_2^f \left(\frac{k_1^f}{A_1^b}\right)^{-1}$ (s^{-1})	$(5.40 \pm 0.35)\ 10^{11}$
$E_a^{\text{global}} = -\Delta H_{\text{ads}}^{\text{CO}} + E_{a,2\text{-f}}$ (kJ mol^{-1})	112.1 ± 7.8

the estimated values with their 95% confidence intervals are shown in Table 5. In Figs. 1 and 2 the CO_2 production rate as calculated by Eq. [13] with the estimated parameter values given in Table 5 is shown together with the experimental data. At large CO and at low O_2 partial pressures the model deviates from the experimental data. An explanation for these model deviations is given in the section "Discussion."

CO Oxidation over Pt/Rh/CeO_2/γ-Al_2O_3 in the Presence of Steam and Carbon Dioxide

A kinetic model, based on elementary steps, was developed for the CO oxidation in the presence of 10 kPa steam and carbon dioxide and $T = 436$ K. At low CO partial pressures, the partial reaction order in CO is less negative as compared to the Pt/γ-Al_2O_3 catalyst, and at high CO partial pressures the order in CO becomes zero. Also, the partial reaction order in O_2 is smaller compared to that of the Pt/γ-Al_2O_3 catalyst. Several explanations can be suggested for these observations. It could be argued that the adsorption properties of the noble metals are altered by the presence of ceria due to electronic interactions. Several TPD and IR studies reported in the literature, however, suggest that the adsorption of CO on the noble metal is not changed by the presence of ceria (25, 46). Moreover, as long as the noble metal is mainly covered with CO, the partial reaction order in CO will remain close to -1 and that in O_2 close to 1. TPD experiments with CO as reducing agent also show production of CO_2 at lower temperatures for catalysts containing both noble metal and ceria as compared to pure ceria. The latter was explained by suggesting reaction between CO adsorbed on the noble metal and oxygen from ceria (26, 28). This second reaction route for the oxidation of CO besides the reaction route catalyzed by the noble metal can explain the less negative order in CO, as compared to the CO oxidation over Pt/γ-Al_2O_3, the zero order in CO at high p_{CO}/p_{O_2}, and the lower partial reaction order in O_2. As this second reaction path comprises both noble metal and ceria sites it is referred to as a bifunctional reaction path. The pathway for CO oxidation catalyzed by the noble metal only, on the other hand, is referred to as a monofunctional reaction path. The elementary reactions considered for describing the bifunctional reaction path are presented in Table 6. No distinction was made between Pt and Rh as both display similar CO oxidation kinetics (17, 19) and both are referred to by the "*" in Table 6, Although 10 kPa of H_2O and CO_2 were fed during the experiments, their influence on the reaction rate is not explicitly taken into account in the elementary reaction steps. The latter is justified because at partial pressures of 10 kPa a small change in the H_2O or CO_2 partial pressure has no significant influence on the reaction rate, as can be seen in Fig. 7. The kinetic model is therefore only valid at 10 kPa of H_2O and CO_2. Reaction paths G, H, and I only differ in the adsorption of oxygen on the ceria sites, denoted by "s." The latter can be sites on top of the ceria lattice, or, more likely, oxygen vacancies at the surface of the ceria lattice.

Step (10) describes the reaction between CO adsorbed on the noble metal surface and oxygen from ceria at the noble metal/ceria interface. In the literature, oxygen spill-over from ceria to the noble metal surface was also suggested (27, 47). This cannot explain the zero-order in CO at high p_{CO}/p_{O_2} as oxygen spillover requires an empty noble metal site. Indeed, the rate expression derived by Mannila *et al.* (47) for a mechanism involving oxygen spillover from ceria to the noble metal surface, followed by a reaction on the noble metal between adsorbed O and adsorbed CO, displays a negative order in CO for large p_{CO}.

For the mechanisms presented in Table 6, diffusion of adsorbed CO on the noble metal and oxygen on the ceria surface or through the ceria lattice toward the noble metal/ceria interface is assumed to be potentially instantaneous. The rate coefficients k_7^f, k_7^b, k_8^f, k_9^f, and k_{10}^f are

TABLE 6

Elementary Step Reaction Paths Considered for the Bifunctional Reaction Path in the Kinetic Modeling of CO Oxidation by O_2 over Pt/Rh/CeO_2/γ-Al_2O_3 in the Presence of H_2O and CO_2. Each Reaction Path G to I Consists of $\{\sigma_{\text{step 1}}, \ldots, \sigma_{\text{step 10}}\}$ Where $\sigma_{\text{step } i}$ Is the Stoichiometric Number for Step i

Elementary step	Reaction path G	Reaction path H	Reaction path I	Step number
	σ_G	σ_H	σ_I	
$CO + * \underset{k_1^b}{\overset{k_1^f}{\rightleftarrows}} CO^*$	2	2	2	(1)
$O_2 + 2s \xrightarrow{k_7^f} 2Os$	1	1	0	(7-f)
$2Os \xrightarrow{k_7^b} O_2 + 2s$	0	1	0	(7-b)
$O_2 + s \xrightarrow{k_8^f} O_2s$	0	0	1	(8)
$O_2s + s \xrightarrow{k_9^f} 2Os$	0	0	1	(9)
$CO^* + Os \xrightarrow{k_{10}^f} CO_2 + * + s$	2	2	2	(10)
$2CO + O_2 \rightarrow 2CO_2$				+

TABLE 7

***F*-Values and Estimates of the Parameters with Their 95% Confidence Intervals Obtained by Regression of the Experimental Data Obtained in the Presence of 10 kPa of H_2O and CO_2 at $T = 436$ K over Pt/Rh/CeO_2/γ-Al_2O_3 with Eqs. [3], [25], and [13], and Eq. [22], [23], or [24]**

Kinetic model	*F*-Value	$2k_3^f\left(\frac{k_1^f}{k_1^b}\right)^{-1}$ /s^{-1}	Parameter corresponding to oxygen adsorption on ceria	k_{10}^f (mol kg_{CAT}^{-1} s^{-1})
Eq. [13] and Eq. [22]	3280	$(3.86 \pm 0.65)\ 10^{-1}$	$k_7^f = (8.8 \pm 3.3)\ 10^{-5}$ [a]	$(7.7 \pm 1.0)\ 10^{-3}$
Eq. [13] and Eq. [23]	3424	$(3.75 \pm 0.68)\ 10^{-1}$	$K_7 = (8.2 \pm 5.8)\ 10^{-3}$ [b]	$(8.5 \pm 1.5)\ 10^{-3}$
Eq. [13] and Eq. [24]	2940	$(4.07 \pm 0.67)\ 10^{-1}$	$k_8^f = (4.85 \pm 1.15)\ 10^{-5}$ [a]	$(6.3 \pm 0.7)\ 10^{-3}$

[a] The unit used is mol kg_{CAT}^{-1} Pa^{-1} s^{-1}.
[b] The unit used is Pa^{-1}.

defined such that the corresponding reaction rate is obtained in the unit mol kg_{CAT}^{-1} s^{-1}. The capacity term(s) concerning reactions involving ceria, e.g., the specific ceria surface, are thus included in the rate coefficients and will therefore not appear explicitly in the reaction rate expressions. This was done because the capacity terms concerning ceria are not known and are difficult to estimate. Remember that the rate coefficients in Table 4 are defined such that the reaction rate is obtained in the unit mol mol_s^{-1} s^{-1} and the specific concentration of active noble metal sites, L_{NM}, appears explicitly in the corresponding rate equations. On the basis of the results obtained with Pt/γ-Al_2O_3 described in the previous section, the rate equations for reaction paths G, H, and I were derived assuming that the noble metal surface is completely covered with CO, i.e., $\theta_{CO} = 1$.

Reaction Path G

In reaction path G the oxygen adsorption on the ceria is assumed to proceed irreversibly and dissociatively in a single reaction step. With the assumption that $\theta_{CO} = 1$, the CO_2 production rate of the bifunctional reaction path, R_{w,CO_2}^{bi}, can be expressed as

$$R_{w,CO_2}^{bi} = k_{10}^f \left[\frac{4k_7^f p_{O_2} + k_{10}^f - \sqrt{8k_7^f k_{10}^f p_{O_2} + \left(k_{10}^f\right)^2}}{4k_7^f p_{O_2}}\right]. \quad [22]$$

Reaction Path H

In reaction path H the oxygen adsorption on the ceria is assumed to proceed reversibly and dissociatively in a single reaction step. With the assumption that $\theta_{CO} = 1$ and that oxygen adsorption is in equilibrium, the CO_2 production rate of the bifunctional reaction path can be expressed as

$$R_{w,CO_2}^{bi} = \frac{k_{10}^f \sqrt{K_7 p_{O_2}}}{\sqrt{K_7 p_{O_2}} + 1}. \quad [23]$$

Reaction Path I

In reaction path I the oxygen adsorption on the ceria is assumed to proceed in two consecutive steps. In step (8), oxygen adsorbs molecularly on a single site, followed by dissociation in step (9). With the assumption that $\theta_{CO} = 1$, and that oxygen adsorption is potentially slow as compared to its dissociation, the CO_2 production rate of the bifunctional reaction path can be expressed as follows:

$$R_{w,CO_2}^{bi} = \frac{2k_8^f k_{10}^f p_{O_2}}{2k_8^f p_{O_2} + k_{10}^f}. \quad [24]$$

The total CO_2 production rate is obtained by summarizing the contributions of the monofunctional path, i.e., Eq. [13], and the bifunctional path, i.e., one of the Eqs. [22]–[24]:

$$R_{w,CO_2}^{tot} = R_{w,CO_2}^{mono} + R_{w,CO_2}^{bi} \quad [25]$$

When using Eq. [22], [23], or [24] for the contribution of the bifunctional path, statistically significant parameter estimates are obtained. The estimates of the different parameters with their 95% confidence limits are given in Table 7. The number of experiments used for the regression is 51. Note that only the overall values at $T = 436$ K can be estimated as all experiments were carried out at this single temperature. From a statistical point of view, Eqs. [22], [23], and [24] are equally suited for describing the experiments, as the *F*-values, also shown in Table 7, do not differ significantly. In Figs. 5a and 6a the measured fractional CO conversion can be compared to the one calculated with the parameters in Table 7 by integration of Eq. [3] using Eq. [13] for the monofunctional reaction path and Eq. [24] for the bifunctional reaction path. The model calculations using Eq. [22] or [23] instead of Eq. [24] are almost identical.

DISCUSSION

For the experimental data obtained with Pt/γ-Al_2O_3 in the absence of steam, Eq. [13] was developed, which corresponds to reaction paths A or B of Table 4, under the

assumptions that molecular adsorption of oxygen is rate determining and CO* is the most abundant reaction intermediate. This indicates that under the experimental conditions molecular adsorption of oxygen rather than the commonly expected (17) direct dissociative chemisorption is the rate-determining step. Another indication for molecular adsorption of oxygen as the rate-determining step is found if the physical significance of the kinetic parameters is assessed. In the rate equation [13] the activation energy consists of the standard CO adsorption enthalpy and the activation energy for oxygen chemisorption. Since molecular chemisorption is essentially unactivated, the activation energy approximately equals $-\Delta H_{\text{ads}}^{\text{CO}}$. The value estimated using Eq. [13] is lower than $-\Delta H_{\text{ads}}^{\text{CO}}$ on an empty Pt surface, which is approximately 125 kJ mol^{-1} (7). However, a surface coverage dependence is often included in CO desorption, i.e., $E_{a,\text{des}}^{\text{CO}} = E_{a,\text{des}}^{\text{CO},0} - \alpha\theta_{\text{CO}}$ (7, 17, 48). In the latter equation, the factor α accounts for the repulsive interaction of adsorbed CO molecules and amounts to 27.2 kJ mol^{-1} (7), which leads to an activation energy of desorption of 97 kJ mol^{-1} for θ_{CO} sufficiently close to unity. The value of E_a^{global} estimated using Eq. [13] is in agreement with this value. Discrimination between paths A and B, i.e., between a Langmuir–Hinshelwood or Eley–Rideal reaction, is not possible on the basis of the present data.

The experimental data obtained with Pt/Rh/CeO_2/γ-Al_2O_3 in the presence of 10 kPa H_2O and CO_2 can be described adequately with the kinetic model consisting of both a monofunctional reaction path, i.e., Eq. [13], and a bifunctional reaction path, i.e., Eq. [22], [23], or [24]. Although Eqs. [22], [23], and [24] are equally adequate from a statistical point of view, Eq. [24] is preferred, because molecularly adsorbed oxygen was demonstrated on ceria surfaces (49–51). Sass *et al.* (49) and Tasarov *et al.* (50) proposed a reaction between this molecularly adsorbed oxygen with CO, resulting in the formation of CO_2 and an adsorbed oxygen atom. The reaction between CO and atomic oxygen was proposed to be substantially faster than with an adsorbed oxygen molecule. The accelerating effect of steam on the reaction rate, as shown in Fig. 7, now may be explained by an increased dissociation rate of molecular oxygen adsorbed on the ceria surface according to the following two reaction steps:

$$H_2O + Os + s \rightleftarrows 2OHs \qquad \text{step (9a)}$$

$$2OHs + O_2s \rightarrow 3Os + H_2O \qquad \text{step (9b)}$$

Note that step (9) of Table 6 is obtained by summarizing step (9a) and (9b). Thus, the overall result of steps (9a) and (9b) is the dissociation of molecular oxygen adsorbed on ceria with no net consumption of H_2O. At 10 kPa of steam, the enhancement of step (9) by steam is apparently such that step (9) can be assumed potentially instantaneous as compared to step (8). Indications for the occurrence of steps (9a) and (9b) were also found in experiments using isotopes (29).

Equations [22]–[24] were derived under the assumption that oxygen diffusion on the ceria surface or through the ceria lattice towards the noble metal/ceria interface is potentially instantaneous. In the Appendix, the rate equation for reaction path I is derived for the case when oxygen diffusion on the ceria surface is taken into account. In the limit of potentially instantaneous surface diffusion, Eq. [24] is obtained. In the limit of slow surface diffusion, Eq. [A6], shown in the Appendix, is obtained. The latter equation is equivalent to Eq. [23], only with a different interpretation of the model parameters. As Eqs. [23] and [24] are equally suited for describing the experiments, no distinction can be made between the two limit cases, fast and slow surface diffusion, on the basis of the experimental data. Also, it can be expected that for intermediate values of the surface diffusion coefficient the experiments can be described equally adequate with Eq. [23] or Eq. [24]. Martin and Duprez (56) determined oxygen surface diffusion coefficients for several oxides. If the surface diffusion coefficient for Rh/CeO_2 is extrapolated to 436 K, a value of 10^{-17} m^2 s^{-1} is obtained. For an estimated diffusion length $L = 1$ nm, a ceria surface capacity $L_{CeO_2} = 0.1$ mol kg$_{\text{CAT}}^{-1}$, $p_{O_2} = 1$ kPa, and the rate coefficients estimated for Eq. [24], shown in Table 7, the full rate Eq. [A5], shown in the Appendix, is close to the limit of potentially instantaneous surface diffusion, i.e. Eq. [24].

The inhibiting effect of CO_2 on the reaction rate, as also shown in Fig. 7, may be explained by the adsorption of CO_2 on ceria, leading to the formation of carboxylate and carbonate species (52). The latter species can decrease the reaction rate of the bifunctional path by decreasing the ceria surface available for oxygen adsorption, by decreasing the concentration of adsorbed oxygen on ceria, by hindering the interface reaction, i.e., step (10), or, if surface diffusion is slow, by decreasing the rate of oxygen surface diffusion. Remember that CO_2 has no significant influence on the CO_2 production rate over Pt/γ-Al_2O_3, i.e., on the monofunctional reaction path.

In Fig. 8, the CO_2 production rate is shown versus p_{O_2} for the Pt/Rh/CeO_2/γ-Al_2O_3 catalyst as calculated with Eq. [25] using Eq. [13] for the monofunctional contribution and Eq. [24] for the bifunctional contribution and using the parameter values given in Table 7. Also, some experimental points are shown. The latter were obtained from experiments with a fractional CO conversion lower than 0.2 under the assumption of differential reactor operation. It can be seen that at low p_{O_2} the CO_2 production rate is almost equal to the contribution of the bifunctional path, while at high p_{O_2} the CO_2 production rate is almost equal to the monofunctional contribution. This can be understood, because at low p_{O_2} the monofunctional contribution becomes very small due to CO inhibition and the oxygen necessary for the oxidation of CO almost exclusively comes from the ceria. At

large p_{O_2} the bifunctional contribution becomes constant while the monofunctional contribution increases linearly with p_{O_2} according to Eq. [13]. Note that the experiments were carried out in the region where both contributions are important. Therefore, statistically significant parameter estimates for both reaction routes could be obtained.

The reason for the accelerating effect of H_2O on the CO oxidation over Pt/γ-Al_2O_3 is not clear. Muraki *et al.* (53) also observed rate enhancement of the CO oxidation over Pt/γ-Al_2O_3 due to the presence of steam. It was suggested that the presence of steam affects the CO adsorption equilibrium, resulting in a decreased CO inhibition, and consequently, higher rates. Another explanation for the rate enhancement by steam could be associated with an increased adsorption rate of oxygen, possibly via the γ-Al_2O_3 support, analogous to the bifunctional path proposed for the Pt/Rh/CeO_2/γ-Al_2O_3 catalyst. The latter can also be an explanation for the model inadequacies of Eq. [13], i.e., the deviations at large values of p_{CO} in Fig. 1 and the deviations at low values of p_{O_2} in Fig. 2. Indeed, a deviation from first order in O_2, at intermediate p_{O_2}, can also be seen in Fig. 8.

Using the estimated preexponential factor and activation energy, given in Table 5, a value of 2×10^{-2} s^{-1} is calculated for the lumped parameter in Eq. [13] for Pt/γ-Al_2O_3 at 436 K. This value is one order of magnitude lower than the value of 4×10^{-1} s^{-1} of the same parameter estimated for Pt/Rh/CeO_2/γ-Al_2O_3 at 436 K, shown in Table 7. For several reasons comparing the parameter estimates for Pt/Rh/CeO_2/γ-Al_2O_3 and Pt/γ-Al_2O_3 is not allowable. First, the experiments with Pt/γ-Al_2O_3 were carried out between 463 to 503 K. Therefore, the estimates in Table 5 are strictly only valid within that temperature region and not at 436 K. Also, the values of the parameter were estimated using the value of L_{NM} measured with CO chemisorption; see Table 1. While for Pt/γ-Al_2O_3 these measurements are rather straightforward, this is not the case for Pt/Rh/CeO_2/γ-Al_2O_3. The value of L_{NM} might be larger than 1.4×10^{-3} mol_s kg_{CAT}^{-1} as used for the calculations, resulting in a lower value of the parameter value of the monofunctional reaction path. Moreover, the experiments with Pt/Rh/CeO_2/γ-Al_2O_3 were carried out in the presence of 10 kPa of H_2O and CO_2, while for Pt/γ-Al_2O_3 the kinetic model was developed for experiments in the absence of H_2O and CO_2. Finally, it must be remembered that for the modeling of the experiments with Pt/Rh/CeO_2/γ-Al_2O_3, no distinction was made between Pt and Rh. Yu Yao (57), however, reported a higher CO oxidation activity for Rh as compared to Pt.

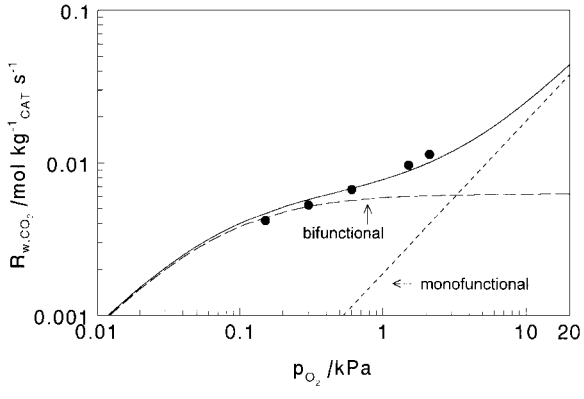

FIG. 8. CO_2 production rate vs p_{O_2} over Pt/Rh/CeO_2/γ-Al_2O_3. $p_{CO} = 0.30$ kPa, $p_{H_2O} = p_{CO_2} = 10$ kPa, $T = 436$ K. Dashed lines show the CO_2 production rate of the monofunctional path, calculated with Eq. [13], and the bifunctional path, calculated with Eq. [24], and the parameter values given in Table 7. The solid line shows the sum of calculated mono- and bifunctional contributions, as in Eq. [25]. Markers represent experimental data.

An important result of the present study is that the rate expression constructed for the "model catalyst" Pt/γ-Al_2O_3 can be applied directly in the model of the more complicated commercial Pt/Rh/CeO_2/γ-Al_2O_3 catalyst. The latter is possible because the rate expressions were derived on the basis of elementary steps, presented in Tables 4 and 6. When using empirical rate expressions, e.g., power-law equations, a new rate expression must be constructed for a new set of experimental data, e.g., a different catalyst. Also, from Fig. 8, it becomes clear that the kinetics of the reaction cannot be characterized simply by a partial reaction order for the different gas phase components. Instead, the dependence of the reaction rate on the partial pressures of the different components depends on the experimental conditions applied.

CONCLUSIONS

The CO oxidation kinetics were studied for a Pt/γ-Al_2O_3 and a commercially available Pt/Rh/CeO_2/γ-Al_2O_3 catalyst in a laboratory fixed-bed microreactor under experimental conditions relevant for automotive exhaust catalysis at temperatures below light-off. For Pt/γ-Al_2O_3 it was concluded that the noble metal surface is almost completely covered with CO and that irreversible molecular adsorption of oxygen is the rate-determining step, followed by potentially instantaneous dissociation. A kinetic model incorporating these features was developed. The presence of steam enhances the reaction rate.

For the Pt/Rh/CeO_2/γ-Al_2O_3 catalyst in the presence of 10 kPa H_2O and CO_2, a kinetic model involving a mono- and bifunctional reaction path was constructed with which the experimental data could be described adequately. The monofunctional reaction path could be described with the same rate expression as obtained for the Pt/γ-Al_2O_3 catalyst. The bifunctional reaction path involves a reaction between CO adsorbed on the noble metal and oxygen from ceria at the noble metal/ceria interface.

The development of the kinetic models on the basis of elementary reaction steps allows the quantification and

understanding of the changes in the partial reaction orders in CO and O_2 as a function of the experimental conditions.

APPENDIX: DERIVATION OF THE RATE EQUATION FOR THE BIFUNCTIONAL PATH I WHEN TAKING OXYGEN SURFACE DIFFUSION INTO ACCOUNT

A ceria surface is considered with a noble metal/ceria interface on both sides. Oxygen adsorbs on the ceria surface, represented by step (8) in Table 6, followed by a potentially instantaneous dissociation, represented by step (9). Next, the adsorbed oxygen atoms diffuse towards the noble metal/ceria interfaces where they react with CO adsorbed on the noble metal surface, represented by step (10) in Table 6. The spatial coordinate on the ceria surface is x [m] and $x=0$ is defined as the middle of the ceria surface. One noble metal/ceria interface is located at $x=L$ and the other at $x=-L$. The steady state continuity equation for oxygen adsorbed on ceria can be represented as

$$D_O \frac{d^2\xi_O}{dx^2} + \beta_8(1-\xi_O) = 0, \qquad [A1]$$

with the boundary conditions

$$x = 0 \qquad \frac{d\xi_O}{dx} = 0 \qquad [A2]$$

$$x = L, x = -L \qquad -D_O \frac{d\xi_O}{dx} = \beta_{10}\xi_O, \qquad [A3]$$

where D_O is the oxygen surface diffusion coefficient [$m^2\ s^{-1}$], ξ_O the degree of surface coverage of oxygen adsorbed on ceria, $\beta_8 = 4k_8^f p_{O_2}/L_{CeO_2}$, $\beta_{10} = 2k_{10}^f L/L_{CeO_2}$, and L_{CeO_2} the monolayer capacity of the ceria surface [mol kg_{CAT}^{-1}].

If Eq. [A1] with boundary conditions [A2] and [A3] is integrated, the following expression for ξ_O at the noble metal interface is obtained:

$$\xi_O(x=L) = \frac{\frac{\sqrt{\beta_8 D_O}}{\beta_{10}} \tanh\left[L\sqrt{\frac{\beta_8}{D_O}}\right]}{1 + \frac{\sqrt{\beta_8 D_O}}{\beta_{10}} \tanh\left[L\sqrt{\frac{\beta_8}{D_O}}\right]}. \qquad [A4]$$

The rate of the bifunctional path can be expressed as follows:

$$R_{w,CO_2}^{bi} = k_{10}^f \xi_O(x=L) = k_{10}^f \frac{\frac{\sqrt{\beta_8 D_O}}{\beta_{10}} \tanh\left[L\sqrt{\frac{\beta_8}{D_O}}\right]}{1 + \frac{\sqrt{\beta_8 D_O}}{\beta_{10}} \tanh\left[L\sqrt{\frac{\beta_8}{D_O}}\right]}. \qquad [A5]$$

In the limit of potentially instantaneous surface diffusion, rate expression [A5] simplifies to Eq. [24]. In the limit of slow surface diffusion, rate expression [A5] simplifies to:

$$R_{w,CO_2}^{bi} = k_{10}^f \frac{\sqrt{\beta_8 D_O}}{\sqrt{\beta_8 D_O} + \beta_{10}} = \frac{\frac{1}{L}\sqrt{k_8^f L_{CeO_2} D_O p_{O_2}}}{\frac{1}{k_{10}^f L}\sqrt{k_8^f L_{CeO_2} D_O p_{O_2}} + 1}. \qquad [A6]$$

ACKNOWLEDGMENT

Degussa A.G. is gratefully acknowledged for providing the catalyst samples.

REFERENCES

1. Weinberg, W. H., and Merril, R. P., *J. Catal.* **40**, 268 (1975).
2. Palmer, R., and Smith, J. N., *J. Chem. Phys.* **60**, 1453 (1974).
3. Engel, T., and Ertl, G., *Chem. Phys. Lett.* **54**, 95 (1978).
4. Engel, T., and Ertl, G., *J. Chem. Phys.* **69**, 1267 (1978).
5. Engel, T., and Ertl, G., *Adv. Catal.* **28**, 1 (1979).
6. Engel, T., *J. Chem. Phys.* **69**, 373 (1978).
7. Herz, R. K., and Marin, S. P., *J. Catal.* **65**, 281 (1980).
8. Boudart, M., and Djéga-Mariadassou, G., "Kinetics of Heterogeneous Catalytic Reactions," Princeton Univ. Press, Princeton, NJ, 1984.
9. McCabe, R. W., Wong, C., and Woo, S. H., *J. Catal.* **114**, 354 (1988).
10. Luntz, A. C., Grimblot, J., and Fowler, D. E., *Phys. Rev. B* **39**, 12903 (1989).
11. Baddour, R. F., Modell, M., and Heusser, U. K., *J. Phys. Chem.* **72**, 3621 (1968).
12. Cant, N. W., Hicks, P. C., and Lennon, B. S., *J. Catal.* **54**, 372 (1978).
13. Bonzel, H. P., and Ku, R., *Surf. Sci.* **40**, 85 (1973).
14. Pacia, N., Cassuto, A., Pentenero, A., and Weber, B., *J. Catal.* **41**, 455 (1976).
15. Golchet, A., and White, J. M., *J. Catal.* **53**, 266 (1978).
16. Campbell, C. T., Ertl, G., Kuipers, H., and Segner, J., *J. Chem. Phys.* **73**, 5862 (1980).
17. Oh, S. H., Fisher, G. B., Carpenter, J. E., and Goodman, D. W., *J. Catal.* **100**, 360 (1986).
18. Boudart, M., and Rumpf, F., *React. Kinet. Catal. Lett.* **35**, 95 (1987).
19. Berlowitz, P. J., Peden, C. H. F., and Goodman, D. W., *J. Chem. Phys.* **92**, 5213 (1988).
20. Voltz, S. E., Morgan, C. R., Liederman, D., and Jacob, S. M., *Ind. Eng. Chem. Prod. Res. Dev.* **12**, 294 (1973).
21. Schlatter, J. C., and Chou, T. S., "71st AlChE Annual Meeting," Paper 66f, 1978.
22. Subramaniam, B., and Varma, A., *Ind. Eng. Chem. Prod. Res. Dev.* **24**, 512 (1985).
23. Montreuil, C. N., Williams, S. C., and Adamczyk, A. A., SAE-paper 920096, 1992.
24. Yao, H. C., and Yu Yao, Y. F., *J. Catal.* **86**, 254 (1984).
25. Oh, S. H., and Eickel, C. C., *J. Catal.* **112**, 543 (1988).
26. Zafiris, G. S., and Gorte, R. J., *J. Catal.* **143**, 86 (1993).
27. Zafiris, G. S., and Gorte, R. J., *J. Catal.* **139**, 561 (1993).
28. Serre, C., Garin, F., Belot, G., and Maire, G., *J. Catal.* **141**, 1 (1993).
29. Campman, M. A. J., "Kinetics of Carbon Monoxide Oxidation over Supported Platinum Catalysts. The Role of Steam in the Presence of Ceria," Ph.D. dissertation. Eindhoven University of Technology, 1996.
30. Engler, B., Koberstein, E., and Schubert, P., *Appl. Catal.* **48**, 71 (1989).
31. Maple, V., release 2, Waterloo Maple software, 1992.
32. Numerical Algorithm Group, "FORTRAN Library Manual, Mark 15," Oxford, 1991.

33. Froment, G. F., and Hosten, L. H., *in* "Catalysis, Science, and Technology" (J. R. Anderson and M. Boudart, Eds.), p. 98. Springer-Verlag, Berlin, 1981.
34. Boggs, P. T., Byrd, R. H., Rogers, J. E., and Schnabel, R. B., "ODRPACK Version 2.01, Software for Weighted Orthogonal Distance Regression," National Institute of Standards and Technology, Gaithersburg, 1992.
35. Kitrell, J. R., *Adv. Chem. Eng.* **8**, 97 (1970).
36. Conrad, H., Ertl, G., and Küppers, J., *Surf. Sci.* **76**, 343 (1978).
37. Solymosi, F., *J. Molec. Catal.* **65**, 337 (1991).
38. Kim, G., *Ind. Eng. Chem. Prod. Res. Dev.* **21**, 267 (1982).
39. Cordatos, H., Bunluesin, T., Stubenrauch, J., Vohs, J. M., and Gorte, R. J., *J. Phys. Chem.* **100**, 785 (1996).
40. Bunluesin, T., Putna, E. S., and Gorte, R. J., *Catal. Lett.* **41**, 1 (1996).
41. Temkin, M. I., *Inter. Chem. Eng.* **11**, 709 (1971).
42. Razon, L. F., and Schmitz, R. A., *Catal. Rev. Sci. Eng.* **28**, 89 (1986).
43. Harold, M. P., and Garske, M. E., *J. Catal.* **127**, 524 (1991).
44. Harold, M. P., and Garske, M. E., *J. Catal.* **127**, 553 (1991).
45. Boudart, M., and Tamaru, K., *Catal. Lett.* **9**, 15 (1991).
46. Zafiris, G. S., and Gorte, R. J., *Surf. Sci.* **276**, 86 (1992).
47. Manilla, P., Salmi, T., Haario, H., Luoma, M., Härkönen, M., and Sohlo, J., *Appl. Catal. B: Environ.* **7**, 179 (1996).
48. Sant, R., and Wolf, E. E., *Chem. Eng. Sci.* **45**, 3137 (1990).
49. Sass, A. S., Shvets, V. A., Savel'eva, G. A., Popova, N. M., and Kazanskii, V. B., *Kinitika i Kataliz* **27**, 894 (1986).
50. Tasarov, A. L., Przheval'skaya, L. K., Shvets, V. A., and Kazanskii, V. B., *Kinitika i Kataliz* **29**, 1181 (1988).
51. Li, C., Kazunari, D., Ken-ichi, M., and Takaharu, O., *J. Am. Chem. Soc.* **111**, 7683 (1989).
52. Li, C., Yoshihisa, S., Totu, A., Kazunari, D., Ken-ichi, M., and Takaharu, O., *J. Chem. Soc., Faraday Trans. 1* **85**, 1451 (1989).
53. Muraki, H., Matunaga, S., Shinjoh, H., Wainwright, M. S., and Trimm, D. L., *J. Chem. Tech. Biotechnol.* **52**, 415 (1991).
54. Dautzenberg, F. M., *ACS Symposium Series*, Vol. 411, p. 99, Amer. Chem. Soc., Providence, RI, 1989.
55. Whittington, B. I., Jiang, C. J., and Trimm, D. L., *Catal. Today* **26**, 41 (1995).
56. Martin, D., and Duprez, D., *J. Phys. Chem.* **100**, 9429 (1996).
57. Yu Yao, Y. F., *J. Catal.* **87**, 152 (1984).